Radiol Phys Technol (2013) 6:210–218
DOI 10.1007/s12194-012-0190-1

Dosimetric properties and clinical application of an a-Si EPID for dynamic IMRT quality assurance

Kenji Matsumoto · Masahiko Okumura · Yoshiyuki Asai · Kouhei Shimomura · Masaya Tamura · Yasumasa Nishimura

Received: 18 July 2012 / Revised: 19 November 2012 / Accepted: 20 November 2012 / Published online: 4 December 2012

Abstract Dosimetric properties of an amorphous silicon electronic portal imaging device (EPID) for verification of intensity-modulated radiation therapy (IMRT) were investigated as a replacement for conventional verification tools. The portal dosimetry system of Varian's EPID (aS1000) has an integrated image mode for portal dosimetry (PD). The source-to-imager distance was 105 cm, and there were no extra buildup materials on the surface of the EPID in this study. Several dosimetric properties were examined. For clinical dosimetry, the dose distributions of dynamic IMRT beams for prostate cancer (19 patients, 97 beams) were measured by EPID and compared with the results of ionization chamber (IC) measurements. In addition, pretreatment measurements for prostate IMRT (50 patients, 309 beams) were performed by EPID and were evaluated by the gamma method (criterion: 3 mm/3 %). The signal-to-monitor unit ratio of PD showed dose dependence, indicating ghosting effects. Tongue-and-groove effects were observed as a result of the dose difference in the measured EPID images. The results of PD for clinical IMRT beams were in good agreement with the predicted dose image with average values of 1.37 and 0.25 for γ_{max} and γ_{ave}, respectively. The point doses of PD were slightly, but significantly, higher than the results of IC measurements ($p < 0.05$ paired t test). However, this small difference seems clinically acceptable. This portal dosimetry system is useful as a rapid and convenient verification tool for dynamic IMRT.

Keywords Portal dosimetry · EPID · IMRT quality assurance

K. Matsumoto (✉) · M. Okumura · Y. Asai · K. Shimomura
Faculty of Medicine, Central Radiological Service,
Kinki University, 377-2 Ohno-higashi, Osaka-Sayama,
Osaka 589-8511, Japan
e-mail: kenji356@me.com

M. Tamura · Y. Nishimura
Faculty of Medicine, Department of Radiation Oncology,
Kinki University, Osaka-Sayama, Japan

1 Introduction

Advanced irradiation techniques, including intensity-modulated radiation therapy (IMRT), require extensive dose verification measurements. The delivery of IMRT beams employs several different techniques, including physical compensators, the step-and-shoot technique [1], and a dynamic multi-leaf collimator (MLC) [2–5]. Verification of dose distributions when these IMRT techniques are used requires at least two-dimensional (2D) dosimetry tools, and has been performed with use of radiographic film [6, 7]. This verification procedure includes recalculation of IMRT plans, set-up of radiographic films on linear accelerators, film processing and digitization, and comparisons of the calculated and measured dose distribution, which is a time-consuming procedure.

Amorphous silicon electronic portal imaging devices (a-Si EPID) were originally designed for patient set-up verification. Because portal images contain dosimetric information, The a-Si EPID has also been used for dose verification recently. 2D verification images can be acquired rapidly without re-entering of the treatment room. 2D detector dosimetry devices have also been proposed based on an ionization chamber or diode array for pretreatment verification of IMRT [8–11]. Whereas good agreement has been reported at specific points or along profiles, these two approaches have limited resolution (0.7–1.4 cm grid spacing) and require additional set-up

time. The EPID has the advantage of higher resolution, and it is already fixed to linear accelerators without needing any additional hardware. Because many radiotherapy departments have invested in portal imagers for patient set-up verification in recent years, it would be useful if the same device could be used also for accurate dose verification.

Early generations of EPIDs consisted of a liquid ion chamber and camera-based fluoroscopic units. The EPID images had poorer contrast and poorer spatial resolution than radiographic films [12–14]. The latest generation of EPIDs has an array of photodiode detectors on an amorphous silicon glass substrate (a-Si EPID). The a-Si EPID produces images that have improved spatial resolution and better contrast than the early generation EPIDs, because the device has an higher detective quantum efficiency.

The dosimetric properties of the a-Si EPID and its applicability to dynamic IMRT verification have been reported [15–21]. One of the approaches to EPID dosimetry was to convert an a-Si EPID image to a dose to water [22]. In this approach, Monte Carlo methods were applied for calculation of the predicted dose distribution at the plane of the EPID. Another approach was the back-projection method, which needs in-house programs for a-Si EPID dosimetry [23]. Each study explored the possibility of EPID dosimetry by use of a special in-house calculation algorithm.

Varian's portal dosimetry (PD) system has image acquisition hardware/software (IDU-20/IAS3) and does not need in-house software for calculation of the predicted dose image (PDI). This commercially available portal dosimetry system was commissioned for the quality assurance (QA) of IMRT treatment plans. Properties investigated were the linearity of the frame number, the linearity of the EPID signal-to-MU ratio, the influence of beam hold-off, the influence of MLC shapes, and the dose accuracy. As for clinical dosimetry, pretreatment verification for the prostate IMRT plan was performed by PD. Our aim in this study was to evaluate the dosimetric properties and application of the PD system as an IMRT verification tool.

2 Methods

An a-Si EPID (aS1000, Varian Medical Systems, Palo Alto, CA) consists of a 1 mm copper metal plate, a 134 mg/cm^2 gadolinium oxysulfide phosphor screen (Kodak, Lanex fast B) that includes a 0.18 mm polyester reflector and a 40 × 30 cm^2 (1,024 × 768 pixels) a-Si array. The 1 mm copper plate is equal to an 8-mm thickness of water and serves as buildup for the incoming radiation. The pixel pitch of aS1000 is 0.39 × 0.39 mm^2 at a source-to-image distance (SID) of 100 cm, which shows higher resolution than that of aS500. The aS1000 was equipped with a Varian 21EX linear accelerator (hereafter abbreviated as 21EX, Varian Medical Systems). 21EX has a Millennium 120 (60 pair) MLC system. Investigations of dosimetric properties and pre-treatment verification of the clinical IMRT plan were performed at an SID of 105 cm without extra buildup materials, with use of a 10 MV photon beam energy and a gantry angle of 0°. The SID of 105 cm is the measurement distance recommended by the manufacturer. The portal dose prediction (PDP) algorithm was implemented in the treatment planning system (TPS). We used the TPS (Varian Eclipse versions 7.3.10 and 10.0.24) to calculate the PDI. Recently, Eclipse was upgraded to version 10.0.24 from version 7.3.10. In the PD system, measured EPID dose images were compared with the PDI calculated from the fluence map of the clinical IMRT plan for verification of the IMRT plan.

2.1 Frame acquisition accuracy

For measurement of EPID dose images, Varian's EPID system uses an integrated image mode. In this study, EPID images were acquired by use of this mode. An EPID image was acquitted as a frame during irradiation. Accumulated frames were displayed as a single dose image after irradiation was completed. The preset rate of frame acquisition was 9.574 frames per second (fps) for 200–600 MU/min and 5.460 fps for 100 MU/min. The image acquisitions were controlled by the central processing unit (CPU) of image acquisition system version 3 (IAS3) located in the treatment room. To verify the accuracy of the frame acquisition by IAS3, we measured the frame number with MU set values of 1–999, and dose rate settings of 200 and 500 MU/min with a 10 × 10 cm^2 open field. For each MU setting, frame was continuously acquired during the irradiation, and they were quantified for each dose rate for analysis.

2.2 Accuracy of the EPID signal-to-MU ratio

The PD system requires several calibrations processes to be used as a dosimetric tool. The calibration procedure was performed according to a calibration protocol recommended by Varian Medical Systems. This calibration procedure has three steps, namely, acquisition of dark-field (DF) images, acquisition of flood-field (FF) images, and dose calibration. First, the DF image was acquired with no radiation and the pixel offsets were recorded. The FF image was recorded with an open-field irradiation (40 × 30 cm^2) for determination of the difference in sensitivity for each pixel. After the acquisition of DF and FF images, an absolute dose calibration was performed. The EPID signal was calibrated with irradiation delivery of 100 MU and a 10 × 10 cm^2 jaw setting. Each calibration

was performed with the dose rate of the verified IMRT plan. Because the PDI was calculated at an SID of 100 cm, a correction factor of 0.907 (i.e., inverse square of SID 105 cm) was applied to the measured EPID signal. The corrected EPID signal was converted to a calibration unit (CU). The CU is a unique absolute-dose unit of the PD (1 CU = 100 MU). The calibration procedure was performed routinely for every measurement.

To investigate the linearity of the signal-to-MU ratio in a range of 1–999 MU, we acquired EPID images using an open square field (10 × 10 cm^2). Two dose rates, 200 and 500 MU/min, were employed. CU values of EPID images were obtained as an average value of a 1 × 1 cm^2 region at the center of the irradiation field. As for the control, ionization chamber (IC) measurements were also performed with the same beam-delivery settings. The cylindrical IC used was a farmer type N30001 model (PTW, Hicksville, NY) of 0.6 cm^3 volume. The IC measurements were recorded in a water tank with the IC positioned at a 2.5-cm water depth and a source-detector distance (SDD) of 102.5 cm. To improve the signal-to-noise ratio, we performed IC measurements at a 2.5-cm water depth (d_{max} of 10 MV). These results were calculated as the signal-to-MU ratio and compared.

The essential factors for EPID-based dosimetry are accuracy of the imager calibration and that of the calculation algorithm of the PDI. To investigate the accuracy of the PDP algorithm, we also calculated the corresponding PDI. Because the PDI can be calculated only for dynamic IMRT fields, a 10 × 10 cm^2 jaw setting and a dynamic MLC moving outside the open field were employed. The CU values of the PDI were also measured as an average value of a 1 × 1 cm^2 area on the central axis. The measured and calculated CU values were compared.

2.3 Response to dose-rate fluctuations

The EPID was calibrated with a fixed dose rate similar to that of the original IMRT plan. When the MLC cannot reach a pre-defined position with maximum leaf speed, the accelerator reduces the dose rate until the MLC reaches a pre-defined position. This phenomenon causes large dose-rate fluctuations during IMRT beam delivery. This phenomenon may affect the measured EPID signals, because this portal dosimetry system is designed and calibrated under a stable dose-rate condition.

Effects of beam hold-offs were examined with use of a stepwise IMRT test pattern. We used two dose-rate settings of 100 and 600 MU/min to deliver the test field with 100 MU. The maximum leaf speed was 2.5 cm/s. Measurements at each dose-rate setting were performed under the same condition as that for the pre-treatment verification measurement. Two profiles along the leaf movement direction in the measured EPID images were obtained and compared.

2.4 Effect of MLC shapes

The MLC has several characteristics such as rounded-leaf-end and tongue-and-groove (T&G) shapes. Several studies investigated the specifications of MLC transmission [24, 25]. At our institution, the rounded-leaf-end transmission value was measured according to the method reported by Arnfield et al. and it was incorporated into the TPS as a calculation parameter. The T&G shape can reduce the transmission passing from each leaf side when the leaves are positioned side by side. However, if a single leaf side contributes to form a radiation field during IMRT irradiation, an unnecessary dose reduction may occur. To evaluate the effects of MLC characteristics on portal dosimetry, we examined a test field using a step-and-shoot

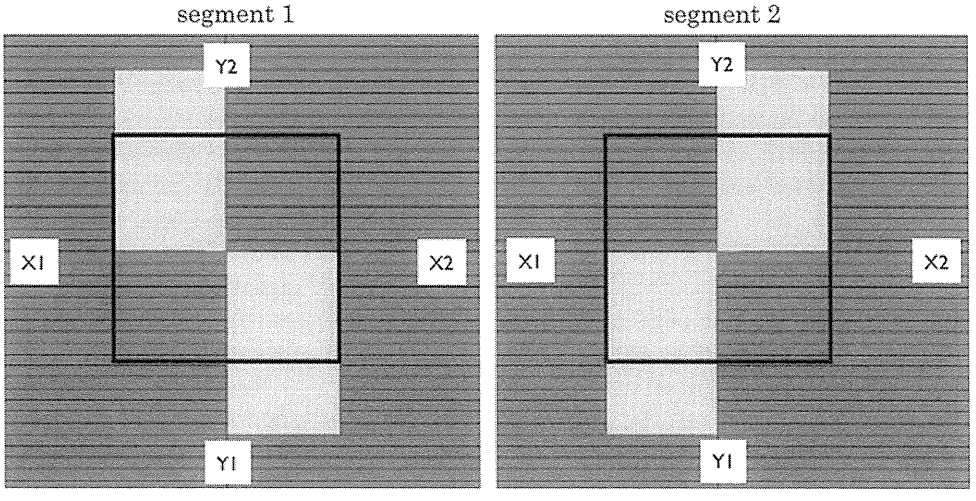

Fig. 1 MLC settings for test fields with 10 × 10 cm^2 jaw sizes. Two segments of MLC were delivered with use of a step-and-shoot IMRT technique

IMRT technique. Two MLC segments were planed sequentially in step-and-shoot mode. The leaf settings of the two segments are shown in Fig. 1. The test field was measured with 100 MU and divided into 50 MU for each segment similar to the pre-treatment verification condition. The PDIs were also calculated by the PDP algorithm of both versions 7.3.10 and 10.0.24. Two dose profiles parallel and perpendicular to the movement direction of the MLC were measured and compared with the PDI.

2.5 Dose accuracy of portal dosimetry

To apply the PD system as a reliable dosimetric tool, it is necessary to confirm whether it has an accuracy equivalent to that of the traditional verification tool. Pre-treatment verification of 19 clinical IMRT plans (97 beams) was performed by EPID and IC. The clinical IMRT plans for the prostate were calculated with use of a dynamic MLC technique, with 5–7 beams of 10 MV X-rays. These were planned by use of a pencil-beam convolution algorithm and a 300 MU/min dose rate so that beam hold-off was avoided. A Farmer type N30001 model (PTW, Hicksville, NY) of 0.6-cm^3 volume was used. To calculate the IC dose, we obtained CT images of a homogeneous IMRT phantom with IC. Each IMRT beam was transposed into the CT image within the TPS. The IC was positioned at high-dose areas in the IMRT dose distribution for improvement of the signal-to-noise ratio. Each IMRT field was recalculated with a gantry angle of 0° and with the same number of MUs as in the original IMRT plan. IC measurements were performed at the same calculation position. The ratio between the IC-measured dose (IC_{meas}) and the TPS-calculated dose ($Plan_{calc}$) was calculated. After EPID calibrations, PD measurements were performed. A point dose on the EPID image was selected at the same position as that of the IC. For every IMRT plan, the verification plan was recalculated by use of PDP algorithm version 7.3.10. The measured EPID doses were compared with the PDI doses. The ratio between the EPID-measured dose ($EPID_{meas}$) and the PDI-calculated dose (PDI_{calc}) was calculated for each beam. Finally, ratios of dose differences for ΔEPID (ΔEPID = $EPID_{meas}/PDI_{calc}$) and ΔIC (ΔIC = $IC_{meas}/plan_{calc}$) were compared and analyzed.

2.6 Clinical application

Pre-treatment verification of 50 prostate IMRT plans with 309 beams was performed by PD. EPID dose images were measured at a gantry angle set to 0° with the original MU. The PDIs were calculated by PDP algorithm version 7.3.10. The measured and calculated dose images were compared by use of the gamma analysis function provided in the Eclipse software [26]. Comparison criteria were set to ±3 % for dose difference and ±3 mm for distance to agreement. The 10 % threshold of the maximum dose was utilized. Maximum gamma (γ_{max}) and average gamma (γ_{avg}) values of 309 IMRT beams were analyzed.

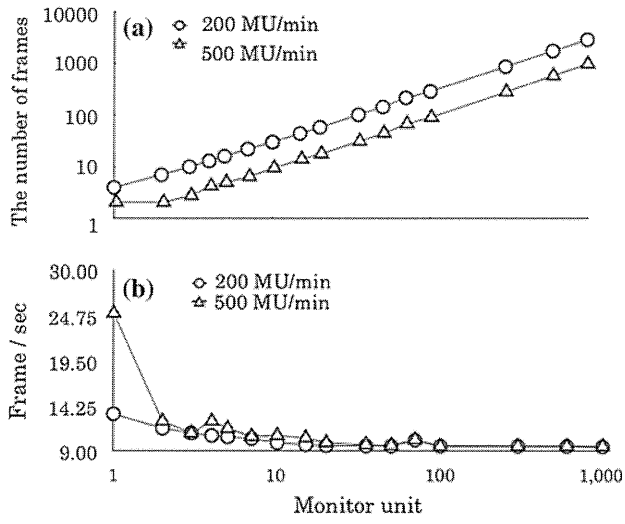

Fig. 2 **a** Linearity of acquired frame number with the monitor unit. Dose rates selected were 200 and 500 MU/min. **b** Frame acquisition rate calculated from the frame number. Preset value of the frame acquisition rate was set as 9.574 fps for each dose rate

3 Results

3.1 Frame acquisition accuracy

The relationship between the number of frames and the MUs delivered is shown in Fig. 2a. Below 3 MU of 500 MU/min, the acquisition frame number per MU was not linear. The frame/s increased up to 25.0. However, this increase in fps was observed only below 3 MU and in high-dose-rate (500 MU/min) beam-delivery situations. The acquisition frame number per MU was stable at 3 MU or more for both dose rates (Fig. 2b).

3.2 Accuracy of the signal-to-MU ratio on EPID

Figure 3 shows signal/MU ratios for EPID and IC. Each ratio was normalized at 100 MU. The signal/MU ratio decreased from 1.0 at MUs of <70. At a high dose rate of 500 MU/min, this tendency was more apparent. In contrast, signal/MU ratios were stable at all MUs for IC. The ghosting effect was observed in the EPID results, and the dependence on the dose rate was identified.

Results for the PDP algorithm calculation accuracy are shown in Fig. 4. The percentage dose differences between measured and calculated CU values were within ±0.5 % at 100 MU or more. Measured CU values of <70 MU were systematically below the calculated CU value. Eventually, in

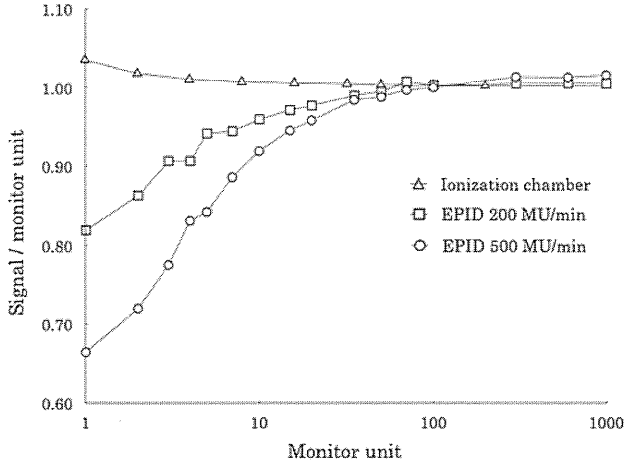

Fig. 3 Signal-to-monitor unit ratios measured by EPID and an ionization chamber. The ionization chamber reading was recorded for determination of the delivery system stability. Each curve was normalized to 1.0 at 100 MU

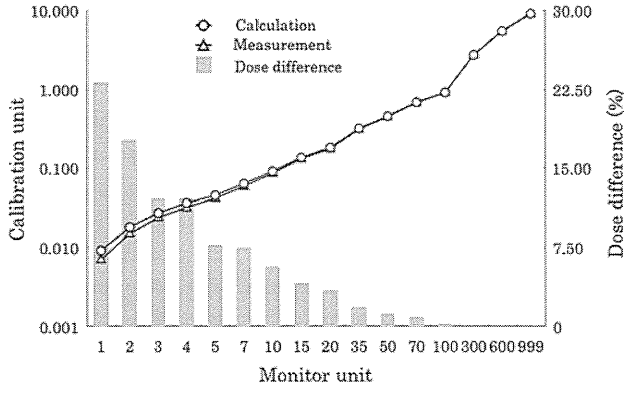

Fig. 4 Calculation accuracy of the PDP algorithm compared with measurements. Dose differences between calculation and measurement are shown as a *bar graph*

PD, combination of ghosting effect and PDP algorithm calculation accuracy was effective on the situation of small MU delivery.

3.3 Response to dose-rate fluctuations

Measured profiles of a test pattern are shown in Fig. 5. The leaf speeds and dose rate were stable during irradiation at 100 MU/min. At a dose rate of 600 MU/min, the dose rate fluctuated between 130 and 600 MU/min when the leaf speed reached 2.5 cm/s. This phenomenon may also occur in clinical IMRT plans. There was no difference in measured CUs at the two different dose rates.

3.4 Effect of MLC shapes

Measured EPID images for the two MLC segments delivered sequentially in step and shoot modes are shown in Fig. 6a. The leaf settings of the two segments are shown in Fig. 1. Profiles perpendicular (inline) and parallel (crossline) to the leaf movement direction are shown in Fig. 6b and c, respectively. Each profile was compared with the calculation by the PDP algorithm. Versions of the PDP calculation algorithm used were 7.3.10 and 10.0.24. On the crossline profile, the dose discrepancy between measured and calculated values for versions 7.3.10 and 10.0.24 was 2.0 and 0.4 %, respectively. The location of this discrepancy just corresponded to the leaf end. This result indicates that the rounded leaf end value employed at our clinic seems correct and was calculated accurately. For the inline profile, calculation of PDP version 7.3.10 did not reflect the T&G effects, and the calculated dose exceeded 21 % of the measured dose (1.4 γ_{max} value). However, with the latest PDP version, 10.0.24, the T&G effect could be calculated.

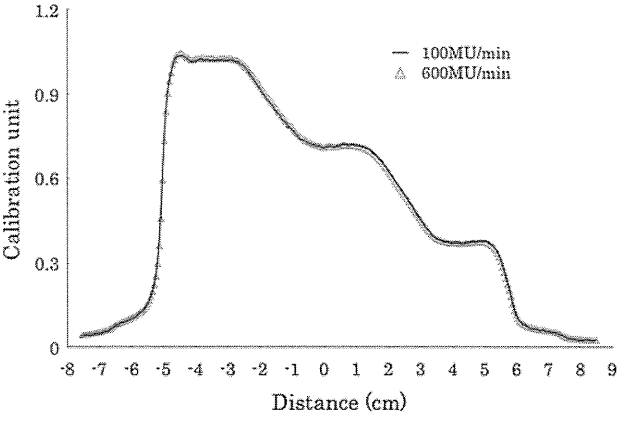

Fig. 5 Effect of dose-rate fluctuations during intensity modulated beam delivery. The stepwise test pattern was delivered by 100 MU at 100 and 600 MU/min. There was beam hold-off during beam delivery of 600 MU/min

3.5 Dose accuracy of portal dosimetry

Point dose differences between PD and IC measurements for 19 prostate IMRT plans with 97 beams are shown in Fig. 7. A positive number indicates that the measured dose was higher than the calculated values. The averaged values of ΔIC and ΔEPID were 0.5 ± 0.9 % (average ± SD) and 1.4 ± 1.0 %, respectively. ΔEPID was systematically and significantly higher than ΔIC ($p < 0.05$, paired t test).

3.6 Clinical application

Histograms of average and maximum γ values for all 309 IMRT beams are shown in Fig. 8. Good agreement between the predicted and measured dose images was observed when we used the 3 mm and 3 % γ criteria. The 10-% threshold was enough to take into account the ghosting effect, because that effect acted on the low-dose

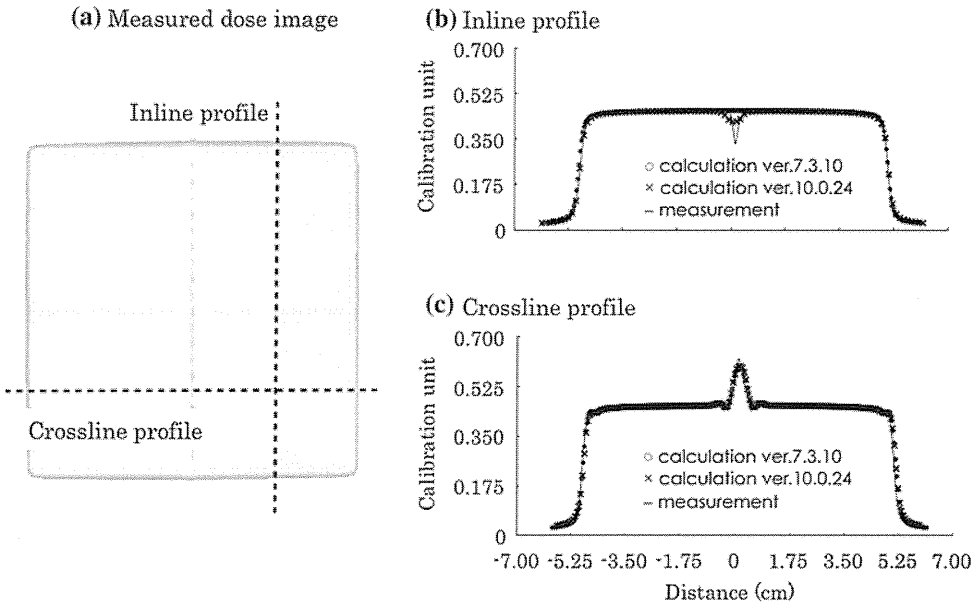

Fig. 6 MLC commissioning test of the PDP calculation algorithm. Two versions were used, 7.3.10 and 10.0.24. **a** Measured dose image of the test IM beam by use of Fig. 1 MLC pattern. **b** Result of inline profile comparing calculated and measured values. **c** Result of crossline profile comparing calculated and measured values

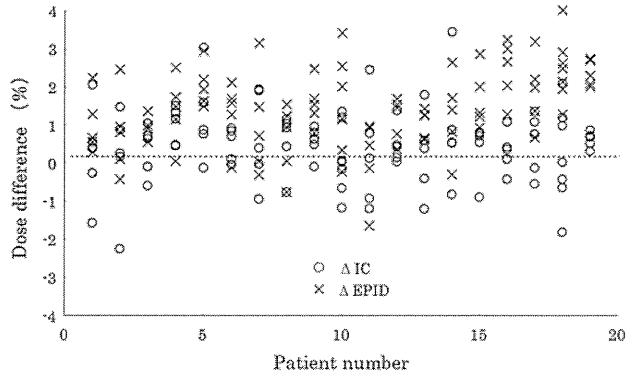

Fig. 7 Point dose difference between PD and IC measurements for 19 prostate IMRT plans (97 beams). Each result was compared with calculated values. A *positive number* indicates that the measured dose was higher than the calculated value

area. The maximum γ_{max} and γ_{avg} of the 309 beams were 3.1 and 0.41, respectively. The average γ_{max} and γ_{avg} of the 309 beams were 1.37 ± 0.42 and 0.26 ± 0.11, respectively. There were 10 fields (3.2 %) with errors of γ_{max} >2.0. In these fields, the measured doses were 6–18 % lower than the calculated dose at small points.

4 Discussion

The present study demonstrated that a PD system could be used for verification of IMRT dose delivery. First, the dosimetric properties of a-Si EPID were investigated. The acquisitioned frame rate was measured, and the acquisition frame number per MU was stable at 3 MU or more for both dose rates (Fig. 2b). The previous image acquisition CPU (IAS2) had a delay between each acquired image due to transfer of the image from the acquisition CPU to the disk and database [15]. This delay (i.e., dead time) was not fixed and could be more than 2.0 s. This delay resulted in image lag (i.e., loss of EPID signal) and inaccurate verification results. The IAS3 performance was different from that of the previous version, and there was no image lag during acquisition. Nonlinearity of the EPID response to MUs was observed in the low-MU region of this portal dosimetry system (Fig. 3). This was consistent with previous reports suggesting that the nonlinearity (known as ghosting effect) depends on the exposure and/or acquisition time [27–29]. The acquisition time dependence or ghosting effects are fundamental properties of the a-Si based EPID.

The calculation accuracy of the PDP algorithm was also investigated. The calculated CU was underestimated in a range of <70 MU. However, in a range of more than 70 MU, the differences between measured and calculated values were within 0.5 %. This result could be due to the fact that the EPID dose calibration was performed at 100 MU. Inaccuracy of the PD in a range of <70 MU may be attributed to a poor EPID response due to ghosting effects in the small-MU region.

Dose-rate fluctuations can occur during IMRT delivery; therefore, it is important to confirm the effect of dose rate fluctuations in PD. Intensity-modulated stepwise test patterns were delivered at 100 and 600 MU/min. Although the dose rate was stable during irradiation at 100 MU/min, it fluctuated between 130 and 600 MU/min when the leaf speed reached 2.5 cm/s. There was no difference in measured CUs at the two dose rates of 100 and 600 MU/min (Fig. 5), which means that dose-rate fluctuation did not affect the PD system.

Modeling of the MLC was commissioned with use of the IMRT test pattern shown in Fig. 1. T&G effects caused

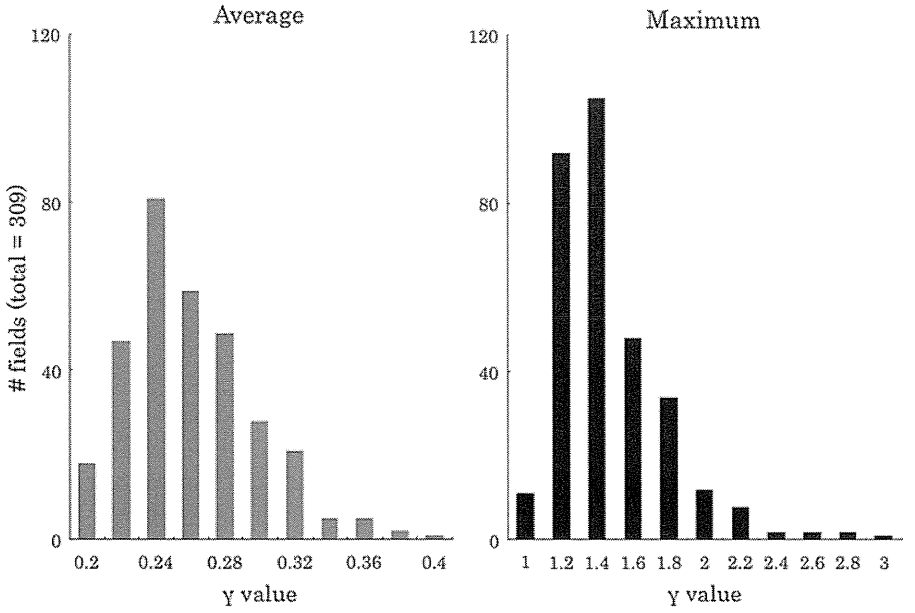

Fig. 8 Histogram of average and maximum γ values with use of 3 mm and 3 % tolerance, for 309 IMRT prostate fields. Measured and calculated dose distributions agreed well overall, with average $\gamma = 0.26$, and maximum $\gamma = 3.0$

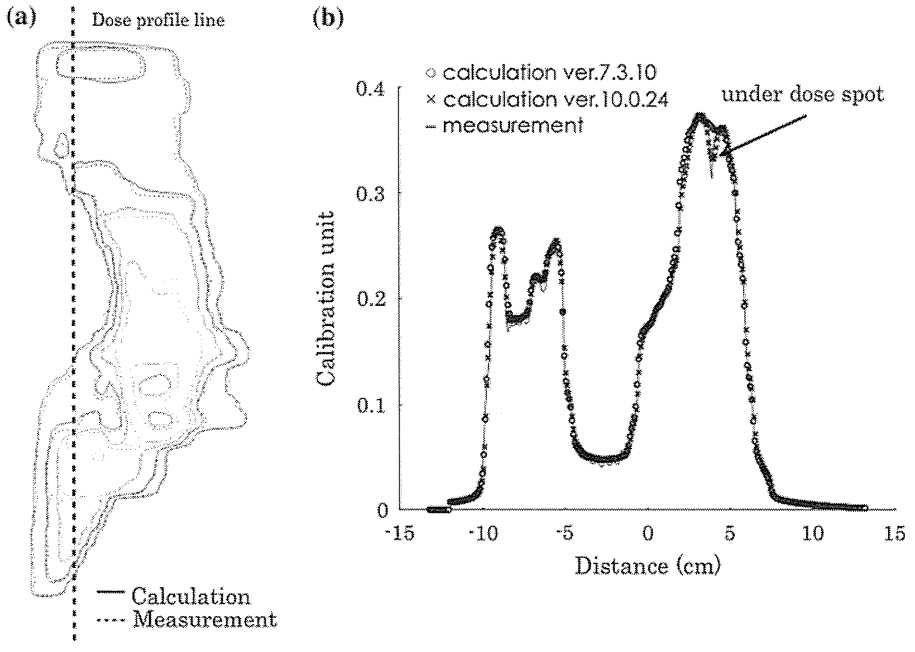

Fig. 9 Results of prostate IMRT verification by use of PDP calculation algorithm versions 7.3.10 and 10.0.24. **a** Measured and calculated dose distribution. *Solid lines* and *dashed lines* are calculation (PDP calculation algorithm version 7.3.10) and measurement, respectively. **b** Comparison of three dose profiles along with the *bold dashed line* in **a**

a large under dosage, and the maximum dose difference was above 20 % in this particular case (Fig. 6). Similar results were observed in our past film measurements. PDP algorithm version 7.3.10 could not calculate the PDI including T&G effects; thus, the gamma value increased when intensity-modulated beams had a single leaf movement. A large discrepancy from T&G effects was occasionally observed in the results of clinical IMRT verification, and an example is shown in Fig. 9. This IMRT treatment plan was used for prostate cancer with metastases of lymph nodes in the pelvis. This plan, therefore, had a large field and more complex leaf movement than ordinary prostate IMRT treatment plans. An under-dose spot was detected in PD, although no under-dose spot was observed in the dose distribution calculated by PDP algorithm version 7.3.10 (Fig. 9b). However, with the PDP calculation algorithm version 10.0.24, T&G effects in PDI can be calculated. T&G effects appear as a line shape moving in the direction of the MLC. Because under-dose spots due to T&G effects can be present in clinical treatment beam delivery, detection of T&G effects is important for quality control of IMRT.

The clinical applicability of PD was investigated with use of clinical IMRT beams for prostate cancer. The point

dose ratios of ΔIC and ΔEPID were 0.5 ± 0.9 % (average ± SD) and 1.4 ± 1.0 %, respectively, with the difference being significant. Although $EPID_{meas}$ was slightly higher than PDI_{calc}, the difference was acceptable clinically. This result suggested that PD is applicable for IMRT verification with the same accuracy as that of IC measurement. As a clinical application of PD, 309 prostate IMRT beams were verified. PDI calculated by PDP algorithm version 7.3.10 was used. The average values of γ_{max} and γ_{avg} were 1.37 ± 0.42 and 0.26 ± 0.11, respectively. Similar values of γ_{max} and γ_{avg} were reported for one PD study [30], and these values seem clinically acceptable. Although 10 fields of γ_{max} >2.0 were noted in the present study, γ_{max} exceeded 2.0 only in a small portion of the fields. Recalculation with PDP calculation version 10.0.24 was performed for the 10 fields, and the maximum gamma value of all 10 fields became γ_{max} <2.0. As the T&G effect was considered in the PDP calculation with version 10.0.24, a more accurate dose distribution was obtained compared with that for PDP algorithm version 7.3.10. Thus, the average gamma values in the present study were within a clinically acceptable range. Our PD system for each IMRT field dose distribution is useful in clarifying the reasons for any error.

In terms of the working time for verification of IMRT, it usually took 5 or 6 h to perform pretreatment IMRT verification with conventional film and IC measurements in our department. After we adopted the PD system, analysis of one clinical IMRT plan could be performed within 30 min. The waiting time between CT scanning for the treatment plan and the start of IMRT was also shortened, from 7 to 4 days.

5 Conclusion

Portal dosimetry including calibration, measurement, and analysis of one clinical IMRT plan could be performed within 30 min; this has a significant positive impact in a busy clinical environment. The PD system is a useful and fast method of dosimetry for both medical staff and patients.

Acknowledgments This study was supported in part by a Grant-in-Aid for Clinical Cancer Research (H23-009) from the Ministry of Health, Labour and Welfare of Japan, and by the National Cancer Center Research and Development Fund (23-A-21).

References

1. Xia P, Verhey LJ. Multileaf collimator leaf sequencing algorithm for intensity modulated beams with multiple static segments. Med Phys. 1998;25(8):1424–34.
2. Convery DJ, Webb S. Generation of discrete beam-intensity modulation by dynamic multileaf collimation under minimum leaf separation constraints. Phys Med Biol. 1998;43(9):2521–38.
3. Spirou SV, Chui CS. Generation of arbitrary intensity profiles by dynamic jaws or multileaf collimators. Med Phys. 1994;21(7):1031–41.
4. Stein J, Bortfeld T, Dorschel B, Schlegel W. Dynamic X-ray compensation for conformal radiotherapy by means of multi-leaf collimation. Radiother Oncol. 2004;32(2):163–73.
5. Wang X, Spirou S, LoSasso T, Stein J, Chui CS, Mohan B. Dosimetric verification of intensity-modulated fields. Med Phys. 1996;23(3):317–27.
6. Bucciolini M, Buonamici FB, Casati M. Verification of IMRT fields by film dosimetry. Med Phys. 2004;31(1):161–8.
7. Ju SG, Ahn YC, Huh SJ, Yeo IJ. Film dosimetry for intensity modulated radiation therapy: dosimetric evaluation. Med Phys. 2002;29(3):351–5.
8. Jursinic PA, Nelms BE. A 2-D diode array and analysis software for verification of intensity modulated radiation therapy delivery. Med Phys. 2003;30(5):870.
9. Poppe B, Blechschmidt A, Djouguela A, Kollhoff R, Rubach A, Willborn KC, et al. Two-dimensional ionization chamber arrays for IMRT plan verification. Med Phys. 2006;33(4):1005–15.
10. Looe HK, Harder D, Ruhmann A, Willborn KC, Poppe B. Enhanced accuracy of the permanent surveillance of IMRT deliveries by iterative deconvolution of DAVID chamber signal profiles. Phys Med Biol. 2010;55(14):3981–92.
11. Poppe B, Looe HK, Chofor N, Ruhmann A, Harder D, Willborn KC. Clinical performance of a transmission detector array for the permanent supervision of IMRT deliveries. Radiother Oncol. 2010;95(2):158–65.
12. Yin FF, Schell MC, Rubin P. Input/output characteristics of a matrix ion-chamber electronic portal imaging device. Med Phys. 1994;21(9):1447–54.
13. Zhu Y, Jiang XQ, Van Dyk J. Portal dosimetry using a liquid ion chamber matrix: dose response studies. Med Phys. 1995;22(7):1101–6.
14. Essers M, Hoogervorst BR, van Herk M, Lanson H, Mijnheer BJ. Dosimetric characteristics of a liquid-filled electronic portal imaging device. Int J Radiat Oncol Biol Phys. 1995;33(5):1265–72.
15. Greer PB, Popescu CC. Dosimetric properties of an amorphous silicon electronic portal imaging device for verification of dynamic intensity modulated radiation therapy. Med Phys. 2003;30(7):1618–27.
16. Greer PB. Correction of pixel sensitivity variation and off-axis response for amorphous silicon EPID dosimetry. Med Phys. 2005;32(12):3558–68.
17. Greer PB, Vial P, Oliver L, Baldock C. Experimental investigation of the response of an amorphous silicon EPID to intensity modulated radiotherapy beams. Med Phys. 2007;34(11):4389–98.
18. Greer PB, Barnes MP. Investigation of an amorphous silicon EPID for measurement and quality assurance of enhanced dynamic wedge. Phys Med Biol. 2007;52(4):1075–87.
19. McCurdy BMC, Greer PB. Dosimetric properties of an amorphous-silicon EPID used in continuous acquisition mode for application to dynamic and arc IMRT. Med Phys. 2009;36(7):3028–38.
20. Gustafsson H, Vial P, Kuncic Z, Baldock C, Denham JW, Greer PB. Direct dose to water dosimetry for pretreatment IMRT verification using a modified EPID. Med Phys. 2011;38(11):6257–64.
21. Sharma DS, Mhatre V, Heigrujam M, Talapatra K, Mallik S. Portal dosimetry for pretreatment verification of IMRT plan: a comparison with 2D ion chamber array. J Appl Clin Med Phys. 2010;11(4):238–48.

22. Warkentin B, Steciw S, Rathee S, Fallone BG. Dosimetric IMRT verification with a flat-panel EPID. Med Phys. 2003;30(12): 3143–55.
23. Wendling M, Louwe RJW, McDermott LN, Sonke J–J, van Herk M, Mijnheer BJ. Accurate two-dimensional IMRT verification using a back-projection EPID dosimetry method. Med Phys. 2006;33(2):259–73.
24. LoSasso T, Chui CS, Ling CC. Physical and dosimetric aspects of a multileaf collimation system used in the dynamic mode for implementing intensity modulated radiotherapy. Med Phys. 1998;25(10):1919–27.
25. Arnfield MR, Siebers JV, Kim JO, Wu Q, Keall PJ, Mohan R. A method for determining multileaf collimator transmission and scatter for dynamic intensity modulated radiotherapy. Med Phys. 2000;27(10):2231–41.
26. Low DA, Harms WB, Mutic S, Purdy JA. A technique for the quantitative evaluation of dose distributions. Med Phys. 1998; 25(5):656–61.
27. McDermott LN, Louwe RJW, Sonke JJ, van Herk MB, Mijnheer BJ. Dose–response and ghosting effects of an amorphous silicon electronic portal imaging device. Med Phys. 2004;31(2):285–95.
28. Winkler P, Hefner A, Georg D. Dose-response characteristics of an amorphous silicon EPID. Med Phys. 2005;32(10):3095–105.
29. McDermott LN, Nijsten SMJJG, Sonke JJ, Partridge M, van Herk M, Mijnheer BJ. Comparison of ghosting effects for three commercial a-Si EPIDs. Med Phys. 2006;33(7):2448–51.
30. Roxby KJ, Crosbie JC. Pre-treatment verification of intensity modulated radiation therapy plans using a commercial electronic portal dosimetry system. Australas Phys Eng Sci Med. 2010; 33(1):51–7.

Journal of Radiation Research, 2013, 54, 1078–1084
doi: 10.1093/jrr/rrt033 Advance Access Publication 14 April 2013

A prospective clinical trial of tumor hypoxia imaging with ^{18}F-fluoromisonidazole positron emission tomography and computed tomography (F-MISO PET/CT) before and during radiation therapy

Izumi TACHIBANA[1,*], Yasumasa NISHIMURA[1], Toru SHIBATA[1], Shuichi KANAMORI[1], Kiyoshi NAKAMATSU[1], Ryuta KOIKE[1], Tatsuyuki NISHIKAWA[1], Kazuki ISHIKAWA[1], Masaya TAMURA[1] and Makoto HOSONO[2]

[1]Department of Radiation Oncology, Kinki University Faculty of Medicine, Osaka-Sayama, Japan
[2]Institute of Advanced Clinical Medicine, Kinki University Faculty of Medicine, Osaka-Sayama, Japan
*Corresponding author. Department of Radiation Oncology, Kinki University Faculty of Medicine, 377-2, Ohno-Higashi, Osaka-Sayama, Osaka 589-8511, Japan. Tel: +81-72-366-0221 (ext. 3132); Fax: +81-72-368-2388; Email: izu917@med.kindai.ac.jp

(Received 31 August 2012; revised 21 March 2013; accepted 22 March 2013)

To visualize intratumoral hypoxic areas and their reoxygenation before and during fractionated radiation therapy (RT), ^{18}F-fluoromisonidazole positron emission tomography and computed tomography (F-MISO PET/CT) were performed. A total of 10 patients, consisting of four with head and neck cancers, four with gastrointestinal cancers, one with lung cancer, and one with uterine cancer, were included. F-MISO PET/CT was performed twice, before RT and during fractionated RT of approximately 20 Gy/10 fractions, for eight of the 10 patients. F-MISO maximum standardized uptake values (SUVmax) of normal muscles and tumors were measured. The tumor-to-muscle (T/M) ratios of F-MISO SUVmax were also calculated. Mean SUVmax ± standard deviation (SD) of normal muscles was 1.25 ± 0.17, and SUVmax above the mean + 2 SD (≥1.60 SUV) was regarded as a hypoxic area. Nine of the 10 tumors had an F-MISO SUVmax of ≥1.60. All eight tumors examined twice showed a decrease in the SUVmax, T/M ratio, or percentage of hypoxic volume (F-MISO ≥1.60) at approximately 20 Gy, indicating reoxygenation. In conclusion, accumulation of F-MISO of ≥1.60 SUV was regarded as an intratumoral hypoxic area in our F-MISO PET/CT system. Most human tumors (90%) in this small series had hypoxic areas before RT, although hypoxic volume was minimal (0.0–0.3%) for four of the 10 tumors. In addition, reoxygenation was observed in most tumors at two weeks of fractionated RT.

Keywords: tumor hypoxia; ^{18}F-misonidazole; PET/CT; reoxygenation

INTRODUCTION

Hypoxic cells of malignant tumors are considered to be radioresistant, and have been regarded as a poor prognostic factor in various cancers [1]. Misonidazole was found to be a hypoxic radiosensitizer by Asquith *et al.* in 1974 [2]. ^{18}F-fluoromisonidazole (F-MISO) was suggested as a tracer to determine hypoxic cells *in vitro* in 1983 [3]. To depict hypoxic lesions in human tumors, many clinical studies using F-MISO Positron Emission Tomography (PET) have been reported since 1991 [4]. In an animal experiment, F-MISO image intensities were inversely correlated with measured intratumoral pO_2 [5].

Over the past 10 years, use of PET/computed tomography (CT) has grown. PET/CT provides relevant information in the staging and therapy monitoring of many tumors because it can give more accurate identification of the anatomical site than PET alone [6]. All F-MISO studies reported before the early 2000s used PET alone instead of PET/CT. For radiation therapy (RT) treatment planning, PET/CT simulation has been used clinically [7], and hypoxic imaging obtained by F-MISO PET/CT may add

some useful information. Although many investigators used the tumor-blood (T/B) ratio, tumor-cerebellum (T/C) ratio, or tumor-to-muscle (T/M) ratio to evaluate intratumoral hypoxia using F-MISO PET with cut-off points of 1.2–1.4 [8–10], no study showed a hypoxic area threshold as an absolute value of F-MISO standardized uptake values (SUV). In the present study, 10 initial patients with various tumors were analyzed to determine a threshold value of SUVmax of F-MISO PET for intratumoral hypoxic areas, and to visualize their reoxygenation during fractionated RT in various human tumors. Also, the appropriate timing of F-MISO PET imaging after F-MISO injection was determined.

MATERIALS AND METHODS

Patients

Between November 2009 and April 2011, 10 patients scheduled for RT for primary or recurrent tumors were enrolled in this prospective study. Eligible patients had histologically proven malignant tumors, with a performance status (PS) level of 0–1 and were aged 20–80 years. Patients without gross target volume, pregnant or lactating women, and patients with mental disorders or severe organ disorders were excluded. Patient and tumor characteristics are summarized in Table 1. Ten patients, consisting of four with head and neck cancers, four with gastrointestinal cancers, one with non-small-cell lung cancer, and one with uterine body cancer, were included. The initial tumor response for both primary tumors and metastatic lymph nodes was evaluated by CT, magnetic resonance imaging (MRI), and clinical examination 1–2 months after the end of treatment according to the RECIST criteria (version 1.1) [11]. Because some tumors regress slowly, tumor response was evaluated at the maximum tumor regression between 1 and 2 months of treatment.

The study protocol was approved by the ethical committee of the Kinki University Faculty of Medicine. All patients signed informed consent before entering the study.

F-MISO and ^{18}F-fluoro-2-deoxyglucose PET/CT protocol

Each patient was scanned with an integrated PET/CT unit (Biograph/Somatom Emotion Duo, Siemens Medical Solutions, Hoffmann Estates, IL, USA). All PET images were acquired using a matrix of 128 × 128 pixels. The time for one bed position (162 mm in z-direction) scan was 120–150 sec. At a distance of 10 cm from the center of the field of view (FOV), the full-width at half maximum (FWHM) reached 7.4 mm × 7.4 mm × 7.1 mm, in the x, y and z directions, respectively. Voxel dimensions were 4.5 mm × 4.5 mm × 2.0 mm. CT scans were acquired in the spiral mode, with a slice thickness of 2–5 mm, a pitch of 6 mm, 130 kv and 55 mAs. The translation speed of the couch was 7.4 mm/sec. As a protocol, F-MISO PET/CT was performed twice before RT and during fractionated RT of ~ 20 Gy/10 fractions. Patients were injected intravenously with 7.4 MBq/kg of F-MISO. No fasting period before F-MISO injection was required. PET/CT was obtained twice, at 100 and 180 min after injection of F-MISO.

F-MISO was synthesized as described previously [12]. In short, in an automated synthesizer (F121, Sumitomo Heavy Industries, Ltd Tokyo, Japan), 5 mg of the precursor 1-(2′-nitro-1′imidazolyl)-2-O-tetrahydropyranyl-3-O-osylpropanediol (NITTP, ABX, Montpellier, France) in 0.3 ml of acetonitrile was reacted with a mixture of dried 18F-fluoride, 7.5 mg of Kryptofix 222 (Merck, Whitehouse Station, NJ, USA), and 2.77 mg of K2CO3 at 110°C for 10 min. After hydrolysis with 0.3 ml of 1N HCl at 80°C for 10 min, 0.6 ml of 1N sodium acetate was added for

Table 1. Patients and tumor characteristics

No.	Age/Sex	PS	Primary site	Stage/Histology	Tumor length	RT dose	Chemotherapy
1	75/M	1	Maxilla sinus	T4a N1 M0/Sq	65 mm	42Gy/21fr[a]	CDDP, 5-FU
2	72/M	0	Esophagus	T3 N1 M0/Sq	30 mm	60Gy/30fr	CDDP, 5-FU
3	60/F	0	Uterine body	recurrence/Ad	48 mm	64.4Gy/35fr	none
4	46/M	0	Nasopharynx	T3 N2c M0/Sq	35 mm	70Gy/35fr	CDDP
5	57/M	0	Lung	T4 N3 M0/Sq	68 mm	60Gy/30fr	Nimotuzumab, CDDP, VNR
6	73/M	0	Esophagus	T3 N2 M0/Sq	28 mm	50Gy/25fr[b]	CDDP, 5-FU
7	72/F	0	Anal canal	T2 N0 M0/Sq	45 mm	59.4Gy/33fr	5-FU, MMC
8	72/M	0	Nasopharynx	T1 N2b M0/Sq	16 mm	70Gy/35fr	CDDP
9	56/M	1	Anal canal	T4 N1 M0/Ad	45 mm	45Gy/25fr[b]	5-FU, MMC
10	36/M	1	Nasopharynx	T4 N1 M0/Sq	42 mm	70Gy/35fr	CDDP

[a]RT was terminated due to severe acute toxicities. [b]Preoperative chemoradiation therapy. Ad = adenocarcinoma, CDDP = cisplatin, 5-FU = fluorouracil, MMC = mitomycin C, Sq = squamous cell carcinoma, VNR = vinorelbine.

neutralization. The product was purified with HPLC chromatography (YMC PAK ODS-AM 10 mm ID × 250 mm, YMC Co., Ltd, Kyoto, Japan) using 3:97 ethanol:H2O, and a 5.0 ml/min flow rate.

For all patients, ^{18}F-fluoro-2-deoxyglucose (FDG) PET/CT was performed before RT. The details of FDG PET/CT at our hospital have been described elsewhere [7].

Radiation therapy and chemotherapy

For all patients, F-MISO PET/CT was performed before the start of RT, but this information was not used for the treatment planning. Eight patients were treated as definitive RT with a planned total dose of 60–70 Gy/30–35 fractions, although one patient terminated RT at 42 Gy due to acute renal failure caused by chemotherapy. The remaining two patients with gastrointestinal cancer were treated with preoperative chemo-RT (CRT) in 45–50 Gy/25 fractions, and curative resection could be done following CRT for these patients. All patients except for a patient with recurrence of uterine body cancer were treated with concurrent chemotherapy. Details of the chemotherapy are summarized in Table 1. During RT, 2–3 cycles of chemotherapy were given.

Analysis

Because normal tissues are considered to be under normoxia, F-MISO SUVs of normal muscles were measured. Data were processed with a Siemens e.soft workstation to measure SUV and hypoxic volume. In placing the volumetric regions of interest (VOIs) over the tumor and normal muscle, the SUVmax of the VOI on PET images was adjusted by referring to CT images and PET/CT fusion images. SUVmax in 108 normal muscle areas was measured for all 18 F-MISO studies. For each study, six oval VOIs of 10–20 cm^3 were measured on bilateral posterior neck muscles (multifidus muscles, semispinalis capitis muscle, and semispinalis cervicis muscle), bilateral back muscles (erector spinae muscle, rhomboid major muscle, and trapezius muscle), or bilateral buttock muscles (gluteus maximus muscle).

For each study, F-MISO SUVmax values of both primary tumors and metastatic lymph nodes of >2cm were measured, and the highest value was regarded as the SUVmax of the study. To calculate the T/M ratio for head and neck tumors, thoracic tumors, or pelvic tumors, the average SUVmax of bilateral posterior neck muscles, back muscles, or buttock muscles was calculated, respectively. For statistical analysis, the paired Student's *t*-test was used to evaluate the difference between 100 min and 180 min after injection of F-MISO.

RESULTS

Eight of the 10 patients underwent FMISO PET/CT twice: before RT and during fractionated RT. One patient refused a second F-MISO PET/CT due to the long examination time, and the other patient's second F-MISO PET/CT was cancelled due to acute renal failure caused by chemotherapy. Changes in SUVmax and the T/M ratio 100 and 180 min after injection of F-MISO in the pretreatment F-MISO study are shown in Table 2. Although large variations in F-MISO SUVmax in tumors were observed between 100 min

Table 2. Changes in SUVmax and T/M ratios at 100 and 180 minutes after injection of F-MISO in pretreatment F-MISO studies

No.	T/M ratio			SUVmax of tumor		
	100 min	180 min		100 min	180 min	
1	1.29	1.93		1.57	2.10	
2	2.66	2.66		2.79	3.06	
3	1.74	1.84		2.99	2.72	
4	1.88	1.86		2.25	2.06	
5	1.59	1.95		1.99	1.60	
6	1.65	2.38		2.33	3.12	
7	1.47	1.77		2.34	2.44	
8	1.22	1.08		1.43	1.35	
9	2.32	1.81		3.82	2.60	
10	1.56	1.61		1.75	1.71	
Tumor	1.74 ± 0.45[a]	1.89 ± 0.42[a]	NS	2.33 ± 0.72[a]	2.28 ± 0.61[a]	NS
Muscle				1.31 ± 0.24[b]	1.25 ± 0.17[b]	p = 0.01

[a]mean ± SD of the 10 tumors. [b]mean ± SD of 108 normal muscle areas.

and 180 min, the mean value of SUVmax was similar for 100 min and 180 min. On the other hand, the mean ± SD of muscle SUVmax decreased significantly 180 min after injection compared to after 100 min ($P = 0.01$). Because of the decrease in the SUVmax of the muscle, the mean value of the T/M ratio at 180 min increased to 1.89 compared with the T/M ratio at 100 min. This means that F-MISO PET/CT images at 180 min had more contrast than those at 100 min. Therefore, we used F-MISO PET/CT imaging 180 minutes after the injection in the present analysis.

To determine the threshold of a hypoxic region, the SUVmax of the 108 areas of normal muscle were measured. The mean ± SD of SUVmax for normal muscle 180 min after F-MISO injection was 1.25 ± 0.17. As the value of the mean + 2 SD was 1.59 SUV, accumulation of F-MISO ≥1.60 was regarded as indicating a hypoxic area. Except for one nasopharyngeal tumor (Fig. 1), nine tumors had F-MISO SUVmax values of ≥1.60 prior to RT, indicating that these tumors contained hypoxic areas before treatment. To obtain high-contrast images and to depict hypoxic areas clearly, the window of F-MISO accumulation was set between 1.6 and 2.0 SUV. In addition, hypoxic volume (HV) was calculated (Table 3). HV was defined as the percentage of hypoxic volume (F-MISO ≥1.60) of the primary tumor or metastatic tumor volume. HV was minimal (0.0–0.3%) for four of the 10 tumors (Table 3). For a patient with nasopharyngeal cancer, no F-MISO accumulation was observed either in the primary tumor or metastatic lymph nodes, although strong FDG uptake was noted (Fig. 1). There was no significant correlation between SUVmax of F-MISO and SUVmax of FDG accumulation for the 10 patients ($r^2 = 0.037$).

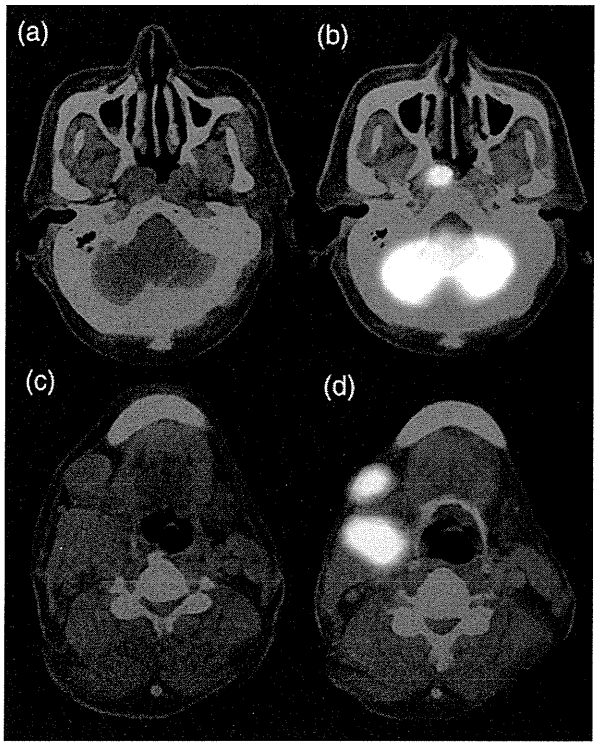

Fig. 1. F-MISO PET/CT (**a**, **c**), and FDG PET/CT (**b**, **d**) for a patient with nasopharyngeal cancer (case 8: T1N2bM0). In this patient, no significant F-MISO accumulation was observed in the primary tumor (SUVmax; 1.20) or metastatic lymph nodes (1.35), although strong FDG uptake was noted.

Reoxygenation of tumors was evaluated in eight tumors on which F-MISO PET/CT studies were performed twice. Six of the eight tumors showed a decrease in SUVmax and/or the T/M ratio at approximately 20 Gy (Fig. 2). The remaining two tumors with increased SUVmax (cases 3 and 9) showed a decrease in HV, while one tumor with decreased SUVmax showed an increase in HV (case 6) (Table 3). Thus, all eight tumors showed a decrease in SUVmax, the T/M ratio, or HV, indicating reoxygenation. Figure 3 shows F-MISO PET/CT of a patient with anal canal squamous cell carcinoma (case 7). In this patient, both SUVmax and HV decreased in the second F-MISO study with 18 Gy/10 fractions.

The results of F-MISO studies and the initial tumor response of the 10 patients are shown in Table 3. In cases 2, 3, 6 and 9, SUVmax of the second F-MISO PET/CT still exceeded 2.5. None of the four tumors showed complete response (CR). On the other hand, four tumors with SUVmax of <2.5 at the second F-MISO PET/CT showed CR or partial response (PR) with long term local control (case 5). Similarly, all four tumors with HV of < 6.0% in the second F-MISO study showed CR or PR with long-term local control.

DISCUSSION

In the present study, the threshold of F-MISO PET for hypoxia was determined as an absolute value of F-MISO SUV. Most previous reports used the T/M ratio or T/B ratio in the definition of tumor hypoxia [8–10]. To introduce F-MISO images to RT planning, a threshold of hypoxia as an absolute value of F-MISO SUV is easy to use. In addition, absolute values of F-MISO SUV can be translated to partial pressure for oxygen (pO_2) based on an experimental study [13]. Another advantage of using absolute values of tumor F-MISO SUV is to eliminate errors in measurements of SUV for normal tissues. We measured the absolute values of F-MISO SUV for many muscle points to determine the range of F-MISO SUV of normal muscles. PET alone has limited spatial resolution compared with PET/CT. Therefore, the PET/CT used in the present study could measure the SUVmax of many areas of normoxic muscle accurately. The threshold for hypoxia was determined to be SUV of F-MISO equal to 1.60 because the mean SUVmax + 2 SD of muscles was 1.59. The range of SUVmax in tumors in this study was 1.35–3.12 with a

Table 3. Changes in F-MISO SUVmax and hypoxic volume (HV) and the initial tumor response

No.	Disease	Treatment	1st-FMISO		2nd-FMISO		Tumor Response
			SUVmax	HV(%)	SUVmax	HV(%)	
1	Maxillary ca.	CRT: 42Gy/21fr	2.10	2.7			PD
2	Esophageal ca.	CRT: 60Gy/30fr	3.06	75.6	2.50	24.6	PR
3	Uterine body ca.	RT: 64.4Gy/35fr	2.72	42.3	3.32	36.5	PR
4	NPC	CRT: 70Gy/35fr	2.06	0.3	1.43	0.0	CR
5	Lung ca.	CRT: 60Gy/30fr	1.60	0.0	1.70	0.0	PR[a]
6	Esophageal ca.	CRT: 50Gy/25fr	3.12	6.7	2.69	7.9	NC
7	Anal canal ca.	CRT: 59.4Gy/33fr	2.44	7.6	.08	2.2	CR
8	NPC	CRT: 70Gy/35fr	1.35	0.0			CR
9	Anal canal ca.	CRT: 45Gy/25fr	2.60	65.8	3.16	6.1	PR
10	NPC	CRT: 70Gy/35fr	1.71	0.1	1.32	0.0	CR

[a]Although the tumor response evaluated by the RECIST criteria was PR, local control was achieved for >2 years.

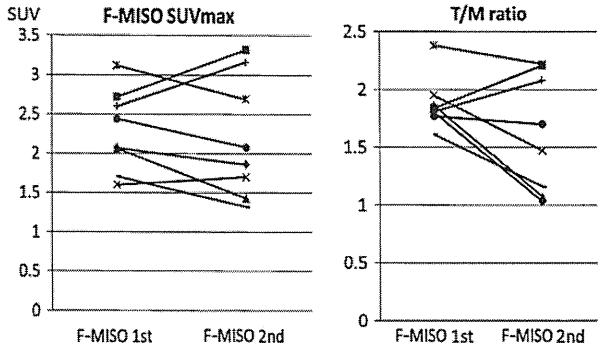

Fig. 2. Changes in F-MISO SUVmax and T/M ratios for eight patients. Six of the eight tumors showed a decrease in SUVmax and/or the T/M ratio after approximately 20 Gy of fractionated RT.

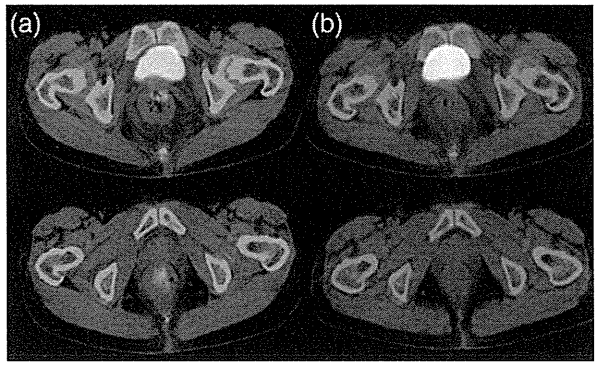

Fig. 3. F-MISO PET/CT (**a**) before RT, and (**b**) during RT (18 Gy/10 fractions), for a patient with anal canal squamous cell carcinoma (case 7: T2N0M0). In this patient, F-MISO accumulation in the primary tumor (SUVmax; 2.44) decreased to 2.08 in the second F-MISO study at 18 Gy/10 fractions.

median of 2.1, which is similar to other previous reports [14, 15].

SUVmax of muscles decreased significantly at 180 min after injection of F-MISO compared with that at 100 min. This may be attributable to the fact that F-MISO in tumor hypoxic areas exhibits slow clearance due to its high lipophilicity. Because of the difference in accumulation and clearance of F-MISO between tumors and normal tissues, it has been reported that the T/M ratio increased up to 3 h after injection of F-MISO [10, 16]. This means that F-MISO PET/CT images at 180 min had more contrast than those at 100 min. Therefore, we used F-MISO PET/CT imaging 180 min after the injection in the present analysis.

In terms of oxygen tension in F-MISO-accumulated areas, one animal experiment using a pig liver showed that F-MISO preferentially binds when pO_2 is < 15 mmHg [13]. In that study, the F-MISO SUV of 1.57 corresponded to a pO2 of 20 mmHg. Therefore, F-MISO-accumulated areas with a threshold of 1.6 SUV in the present study may represent hypoxic areas with a pO_2 of <20 mmHg. The oxygen enhancement ratio (OER) was approximately 3 under well-oxygenated conditions and it decreased for pO_2 below 20 mmHg [17]. The OER decreased to 2.0–2.8 at an oxygen tension of 3–20 mmHg. Thus, the F-MISO-accumulated areas are radioresistant compared with other normoxic regions.

In the present study, SUVmax, the T/M ratio, or HV decreased in all eight tumors after approximately 20 Gy, indicating reoxygenation. It is reported that errors in measurements on SUVmax are approximately 10%, so a decrease in SUVmax of > 10% may be significant [18, 19]. Except for case 5, the decrease in SUVmax was > 10% for the eight tumors (Table 3). Notably, for case 9, SUVmax increased in the second F-MISO study (Table 3), although HV decreased to 6% from the initial value of 66%. HV may be a more appropriate indicator for reoxygenation than

SUVmax or the T/M ratio because both SUVmax and the T/M ratio are calculated based on the maximum point SUV. The decrease in F-MISO SUVmax may be related to a decrease in blood flow following vascular damage due to RT. However, it has been demonstrated that the functional vascularity in human tumors remains unchanged or improves slightly during the early period of conventional fractionated RT with 1.5–2.0 Gy daily doses [20]. Therefore, we consider that the decrease in F-MISO accumulation indicates reoxygenation of tumor cells.

The information on tumor hypoxia from F-MISO PET/CT can be used for dose painting intensity modulated radiation therapy planning. Although some reports showed dose painting RT plans up to a maximum tumor dose of 84–105 Gy using F-MISO PET/CT [21, 22], no clinical trials for dose escalation to hypoxic areas have been reported. One reason for not performing such clinical trials is that the reproducibility of intratumor distribution of F-MISO is unclear [23]. Nehmeh *et al.* [24] found that only six of 13 human tumors showed well-correlated intratumor distributions of F-MISO after a three-day interval without treatment. The remaining seven tumors showed different distributions of F-MISO after three days. The other factor is reoxygenation of hypoxic areas during fractionated RT. Therefore, dose escalation to the hypoxic areas in the initial PET/CT before RT may be inappropriate. In the near future, if frequent imaging of F-MISO PET/CT is available, adaptive RT for tumor hypoxia may be used clinically.

F-MISO PET/CT obtained before or during fractionated RT can be used as an independent prognostic measure and has implications for treatment strategy. If tumor response can be predicted at the initial period of RT, the treatment strategy can be changed to a more intensive one or a substitute therapy can be started. In the present study, tumors with an SUVmax of >2.5 or an HV of > 6.0% in the second F-MISO study showed poor local response. Similar results were shown in various reports on head and neck cancer and lung cancer using pretreatment hypoxia imaging [25, 26]. The predictive value of hypoxic imaging should be evaluated in future studies.

In conclusion, accumulation of F-MISO of ≥1.60 SUV was regarded as an intratumoral hypoxic area in our F-MISO PET/CT system. Most human tumors (90%) in this small series had hypoxic areas before RT, although HV was minimal (0.0–0.3%) in four of the 10 tumors. In addition, reoxygenation was observed in most tumors at two weeks of fractionated RT.

FUNDING

This study was supported by a Grant-in-Aid for Scientific Research (22591392, 25461932) from the Ministry of Education, Culture, Sports, Science and Technology, Japan.

REFERENCES

1. Vaupel P, Mayer A. Hypoxia in cancer: significance and impact on clinical outcome. *Cancer Metastasis Rev* 2007;**26**:225–39.
2. Asquith JC, Watts ME, Patel K *et al.* Electron affinic sensitization. V. Radiosensitization of hypoxic bacteria and mammalian cells *in vitro* by some nitroimidazoles and nitropyrazoles. *Radiat Res* 1974;**60**:108–18.
3. Chapman JD, Baer K, Lee J. Characteristics of the metabolism-induced binding of misonidazole to hypoxic mammalian cells. *Cancer Res* 1983;**43**:1523–8.
4. Koh WJ, Rasey JS, Evans ML *et al.* Imaging of hypoxia in human tumors with [F-18]fluoromisonidazole. *Int J Radiat Oncol Biol Phys* 1991;**22**:199–212.
5. Zimny M, Gagel B, DiMartino E *et al.* FDG—a marker of tumour hypoxia? A comparison with [18F]fluoromisonidazole and pO2-polarography in metastatic head and neck cancer. *Eur J Nucl Med Mol Imaging* 2006;**33**:1426–31.
6. von Schulthess GK, Steinert HC, Hany TF. Integrated PET/CT: current applications and future directions. *Radiology* 2006;**238**:405–22.
7. Okubo M, Nishimura Y, Nakamatsu K *et al.* Radiation treatment planning using positron emission and computed tomography for lung and pharyngeal cancers: a multiple-threshold method for [^{18}F]fluoro-2-deoxyglucose activity. *Int J Radiat Oncol Biol Phys* 2010;**77**:350–6.
8. Rasey JS, Koh W, Evans ML *et al.* Quantifying regional hypoxia in human tumors with positron emission tomography of [^{18}F]fluoromisonidazole: a pretherapy study of 37 patients. *Int J Radiat Oncol Biol Phys* 1996;**36**:417–28.
9. Rajendran JG, Wilson DC, Conrad EU *et al.* [(18)F]FMISO and [(18)F]FDG PET imaging in soft tissue sarcomas: correlation of hypoxia, metabolism and VEGF expression. *Eur J Nucl Med Mol Imaging* 2003;**30**:695–704.
10. Koh WJ, Rasey JS, Evans ML *et al.* Imaging of hypoxia in human tumors with [F-18]fluoromisonidazole. *Int J Radiat Oncol Biol Phys* 1991;**22**:199–212.
11. Eisenhauer EA, Therasse P, Bogaerts J *et al.* New response evaluation criteria in solid tumors: revised RECIST guideline (version 1.1). *Eur J Cancer* 2009;**45**:228–247.
12. Tang G, Wang M, Tang X *et al.* Fully automated one-pot synthesis of [18F]fluoromisonidazole. *Nucl Med Biol* 2005;**32**:553–8.
13. Piert M, Machulla HJ, Becker G *et al.* Dependency of the [^{18}F]Fluoromisonidazole uptake on oxygen delivery and tissue oxygenation in the porcine liver. *Nucl Med Biol* 2000;**27**:693–700.
14. Yamane T, Kikuchi M, Shinohara S *et al.* Reduction of [^{18}F] Fluoromisonidazole uptake after neoadjuvant chemotherapy for head and neck squamous cell carcinoma. *Mol Imaging Biol* 2011;**13**:227–31.
15. Eschmann SM, Paulsen F, Bedeshem C *et al.* Hypoxia-imaging with ^{18}F-misonidazole and PET: changes of kinetics during radiotherapy of head-and-neck cancer. *Radiother Oncol* 2007;**83**:406–10.
16. Sørensen M, Horsman MR, Cumming P *et al.* Effect of intratumoral heterogeneity in oxygenation status on FMISO PET,

autoradiography, and electrode Po2 measurements in murine tumors. *Int J Radiat Oncol Biol Phys* 2005;**62**:854–61.
17. Hall EJ. Radiobiology for the Radiologist. 6th edn. Philadelphia: Lippincott Williams and Wilkins, 2006, pp. 88–89.
18. Nahmias C, Wahl LM. Reproducibility of standardized uptake value measurements determined by 18F-FDG PET in malignant tumors. *J Nucl Med* 2008;**49**:1804–08.
19. Kinahan PE, Fletcher JW. Positron emission tomography–computed tomography standardized uptake values in clinical practice and assessing response to therapy. *Semin Ultrasound CT MR* 2010; **31**:496–505.
20. Park HJ, Griffin RJ, Hui S *et al.* Radiation-induced vascular damage in tumors: implications of vascular damage in ablative hypofractionated radiotherapy (SBRT and SRS). *Radiat Res* 2012;**177**:311–27.
21. Lee NY, Mechalakos JG, Nehmeh S *et al.* Fluorine-18-labeled fluoromisonidazole positron emission and computed tomography-guided intensity-modulated radiotherapy for head and neck cancer: a feasibility study. *Int J Radiat Oncol Biol Phys* 2008;**70**:2–13.
22. Choi W, Lee SW, Park SH *et al.* Planning study for available dose of hypoxic tumor volume using fluorine-18-labeled fluoromisonidazole positron emission tomography for treatment of the head and neck cancer. *Radiother Oncol* 2010;**97**:176–82.
23. Lin Z, Mechalakos J, Nehmeh S *et al.* The influence of changes in tumor hypoxia on dose-painting treatment plans based on ^{18}F-FMISO positron emission tomography. *Int J Radiat Oncol Biol Phys* 2008;**70**:1219–28.
24. Nehmeh SA, Lee NY, Schroder H *et al.* Reproducibility of intratumor distribution of ^{18}F-fluoromisonidazole in head and neck cancer. *Int J Radiat Oncol Biol Phys* 2008;**70**:235–42.
25. Dirix P, Vandecaveye V, De Keyzer F *et al.* Dose painting in radiotherapy for head and neck squamous cell carcinoma: value of repeated functional imaging with (18)F-FDG PET, (18)F-fluoromisonidazole PET, diffusion-weighted MRI, and dynamic contrast-enhanced MRI. *J Nucl Med* 2009;**50**:1020–7.
26. Rajendran JG, Schwartz DL, O'Sullivan J *et al.* Tumor hypoxia imaging with [F-18]Fluoromisonidazole positron emission tomography in head and neck cancer. *Clin Cancer Res* 2006;**12**:5435–41.

Cancer Medicine

Open Access

ORIGINAL RESEARCH

Human papillomavirus DNA and p16 expression in Japanese patients with oropharyngeal squamous cell carcinoma

Hisato Kawakami[1], Isamu Okamoto[1,2], Kyoichi Terao[3], Kazuko Sakai[4], Minoru Suzuki[5], Shinya Ueda[1], Kaoru Tanaka[1], Kiyoko Kuwata[1], Yume Morita[1], Koji Ono[5], Kazuto Nishio[4], Yasumasa Nishimura[6], Katsumi Doi[3] & Kazuhiko Nakagawa[1]

[1]Department of Medical Oncology, Kinki University Faculty of Medicine, 377-2 Ohno-higashi, Osaka-Sayama, Osaka 589-8511, Japan
[2]Center for Clinical and Translational Research, Kyushu University Hospital, 3-1-1 Maidashi, Higashiku, Fukuoka 812-8582, Japan
[3]Department of Otolaryngology, Kinki University Faculty of Medicine, 377-2 Ohno-higashi, Osaka-Sayama, Osaka 589-8511, Japan
[4]Department of Genome Biology, Kinki University Faculty of Medicine, 377-2 Ohno-higashi, Osaka-Sayama, Osaka 589-8511, Japan
[5]Radiation Oncology Research Laboratory, Research Reactor Institute, Kyoto University, Sennan-gun, Osaka 590-0494, Japan
[6]Department of Radiation Oncology, Kinki University Faculty of Medicine, 377-2 Ohno-higashi, Osaka-Sayama, Osaka 589-8511, Japan

Keywords
DNA methylation, human papillomavirus, oropharynx, p16, squamous cell carcinoma

Correspondence
Isamu Okamoto, Center for Clinical and Translational Research, Kyushu University Hospital, 3-1-1 Maidashi, Higashiku, Fukuoka 812-8582, Japan.
Tel: +81-92-642-5378; Fax: +81-92-642-5390;
E-mail: okamotoi@kokyu.med.kyushu-u.ac.jp

Funding Information
This study was supported in part by a Grand-in-Aid for Cancer Research (H23-009) from the Ministry of Health, Labor, and Welfare of Japan.

Received: 14 August 2013; Revised: 18 September 2013; Accepted: 18 September 2013

Cancer Medicine **2013; 2(6): 933–941**

doi: 10.1002/cam4.151

Abstract

Human papillomavirus (HPV) is a major etiologic factor for oropharyngeal squamous cell carcinoma (OPSCC). However, little is known about HPV-related OPSCC in Japan. During the study, formalin-fixed, paraffin-embedded OPSCC specimens from Japanese patients were analyzed for HPV DNA by the polymerase chain reaction (PCR) and for the surrogate marker p16 by immunohistochemistry. For HPV DNA-positive, p16-negative specimens, the methylation status of the p16 gene promoter was examined by methylation-specific PCR. Overall survival was calculated in relation to HPV DNA and p16 status and was subjected to multivariate analysis. OPSCC cell lines were examined for sensitivity to radiation or cisplatin in vitro. The study results showed that tumor specimens from 40 (38%) of the 104 study patients contained HPV DNA, with such positivity being associated with tumors of the tonsils, lymph node metastasis, and nonsmoking. Overall survival was better for OPSCC patients with HPV DNA than for those without it (hazard ratio, 0.214; 95% confidence interval, 0.074–0.614; $P = 0.002$). Multivariate analysis revealed HPV DNA to be an independent prognostic factor for overall survival ($P = 0.015$). Expression of p16 was associated with HPV DNA positivity. However, 20% of HPV DNA-positive tumors were negative for p16, with most of these tumors manifesting DNA methylation at the p16 gene promoter. Radiation or cisplatin sensitivity did not differ between OPSCC cell lines positive or negative for HPV DNA. Thus, positivity for HPV DNA identifies a distinct clinical subset of OPSCC with a more favorable outcome in Japanese.

Introduction

Head and neck cancer is the sixth most common cancer worldwide, with an estimated annual incidence of approximately 600,000 cases [1]. Although the incidence of such cancer overall has fallen in recent years, consistent with the decrease in tobacco use, that of oropharyngeal squamous cell carcinoma (OPSCC) has increased in both the United States and Europe. In 2009, the International Agency for Research on Cancer recognized human papillomavirus (HPV) type 16 as a causal agent of OPSCC [2]. Individuals with HPV-positive OPSCC show significantly better overall survival and disease-free survival, associated with a 20–80% reduction in the risk of death, compared with those with HPV-negative OPSCC [3, 4]. Knowledge of HPV status in patients with OPSCC is thus expected to play an increasing role in the management of this disease. Epidemiological evidence from several countries indicates that the proportion of OPSCC cases caused by HPV varies widely, however. Although the proportion of

OPSCC cases attributable to HPV ranges from 40 to 80% in the United States and is around 90% in Sweden [3, 5], little is known about HPV-related OPSCC in Asian populations.

The aim of this study was to evaluate the prevalence, clinical features, and outcome of OPSCC positive for HPV DNA in the Japanese population. We also assessed the concordance between the presence of HPV DNA in tumor specimens and expression of the host cyclin-dependent kinase inhibitor p16 as detected by immunohistochemistry (IHC), given that p16 is commonly examined as a surrogate marker for HPV positivity in OPSCC [3, 6], and we further investigated possible mechanisms underlying any discordance. Moreover, to evaluate the biological impact of HPV infection, we examined the sensitivity of OPSCC cell lines positive or negative for HPV DNA to radiation and to cisplatin.

Material and Methods

Patients and tissue

With approval of the appropriate institutional review board, we analyzed formalin-fixed, paraffin-embedded (FFPE) tissue from 118 consecutive patients with newly diagnosed and histologically confirmed OPSCC who were treated at Kinki University Hospital from November 2000 through December 2011. Tumor specimens for all cases were obtained during surgery or diagnostic biopsy, and one representative paraffin block was selected for each case. Several 6-μm paraffin sections were used for analysis of HPV DNA, and one 3-μm section was used for p16 IHC. Patients without sufficient tumor tissue available for both analysis of HPV DNA and p16 staining were excluded, leaving 104 patients in the study (Fig. 1).

Clinicopathologic characteristics and outcome data for patients were obtained from the medical records. Treatment modality was selected for each patient individually on the basis of the official published guidelines. Most individuals underwent radiation therapy or radiochemotherapy according to a standard fractionated regimen, receiving 60–70 Gy with or without concomitant platinum-based chemotherapy. Adjuvant radiotherapy (54–64 Gy) was administered with standard fractionation.

Analysis of HPV DNA

The FFPE specimens were depleted of paraffin and then subjected to macrodissection in order to select a region of cancer tissue. Genomic DNA was extracted from the cancer tissue with the use of a QIAamp DNA Micro Kit (Qiagen, Hilden, Germany), and the DNA concentration of each extract was determined with a NanoDrop 2000 spectrophotometer (Thermo Scientific, Waltham, MA). DNA for HPV types 16, 18, 31, 33, and 35 was detected with the use of a TaqMan real-time polymerase chain reaction (PCR)-based method (Applied Biosystems, Foster City, CA) that was designed to amplify the E6 region or E7 region (or both) of the viral genome. The primer and probe sequences for amplification have been described previously [7–9]. Samples of genomic DNA that had sufficient amplifiable β-globin DNA (>1 human genome/μL) were considered to be evaluable, and HPV type was determined for β-globin gene-positive and HPV DNA-positive specimens. We defined active HPV DNA

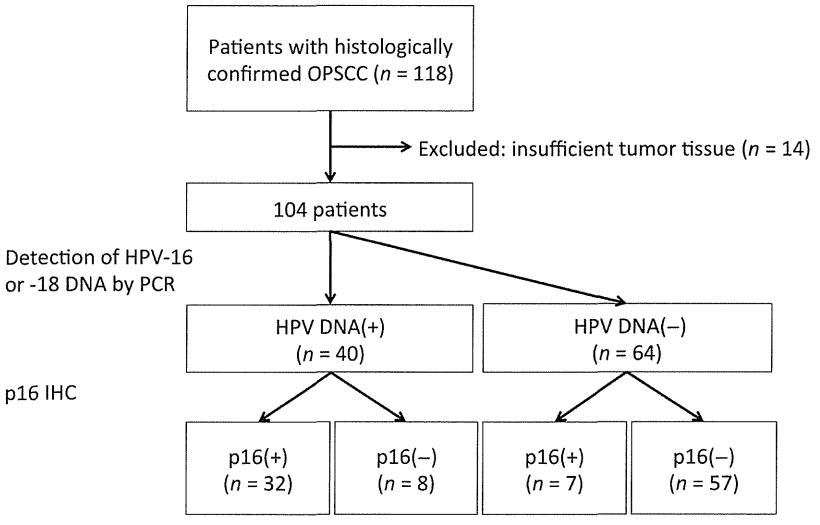

Figure 1. Summary of the protocol for classification of enrolled OPSCC patients according to HPV DNA and p16 status. OPSCC, oropharyngeal squamous cell carcinoma; HPV, human papillomavirus.

involvement as PCR detection at the level of at least one copy per 10 cell genomes [7]. PCR analysis was performed in duplicate.

IHC for detection of p16 expression

Immunohistochemistry for p16 was performed with the use of a CINtec Histology Kit (MTM Laboratories AG, Heidelberg, Germany) based on the monoclonal antibody E6H4. A tonsil squamous cell carcinoma with a high level of p16 expression was used as a positive control, and the primary antibody was omitted as a negative control. Expression of p16 was scored positive if strong and diffuse nuclear and cytoplasmic staining was present in >70% of the tumor cells [10], and p16 scoring was performed without knowledge of HPV status. Representative p16 IHC images are shown in Figure 2.

Methylation-specific-PCR analysis

For assessment of DNA methylation at the p16 gene promoter, genomic DNA samples were subjected to sodium bisulfite modification with the use of a MethylEasy Xceed Rapid DNA Bisulfite Modification Kit (Human Genetic Signatures, Randwick, NSW, Australia). The modified DNA was then used as a template for methylation-specific (MS)-PCR with primers specific for methylated or unmethylated sequences [11]. The sizes of the MS-PCR products were previously described [12]. Real-time MS-PCR analysis was performed in a 25-μL reaction mixture with the use of an EpiScope MSP Kit (Clontech, Mountain View, CA). EpiScope Methylated HCT116 gDNA and EpiScope Unmethylated HCT116 DKO gDNA (Clontech) were used as positive and negative controls, respectively.

Cell culture

The human OPSCC cell lines UPCI-SCC-003, UPCI-SCC-036, UPCI-SCC-089, UPCI-SCC-090, UPCI-SCC-152, and UPCI-SCC-154 were kindly provided by S. Gollin (University of Pittsburgh School of Public Health, Pittsburgh, PA). The cells were cultured under an atmosphere of 5% CO_2 at 37°C in Dulbecco's modified Eagle's medium (Sigma-Aldrich, St Louis, MO) supplemented with 10% heat-inactivated fetal bovine serum (Hyclone, Logan, UT), 0.1 mmol/L nonessential amino acids (Gibco-Invitrogen, Carlsbad, CA), 2 mmol/L L-glutamine, and 1 mmol/L sodium pyruvate (Sigma-Aldrich).

Clonogenic survival assay

Exponentially growing cells in 25-cm^2 flasks were harvested by exposure to trypsin and counted. They were diluted serially to appropriate densities, plated in triplicate in 25-cm^2 flasks containing 10 mL of complete medium, and exposed at room temperature to various doses of radiation with a ^{60}Co irradiator at a rate of ~0.82 Gy/min. The cells were cultured for 14–21 days, fixed with methanol:acetic acid (10:1, v/v), and stained with crystal violet. Colonies containing >50 cells were counted. The surviving fraction was calculated as: (mean number of colonies)/(number of plated cells × plating efficiency). Plating efficiency was defined as the mean number of colonies divided by the number of plated cells for corresponding nonirradiated cells.

Cell growth inhibition assay

Cells were transferred to 96-well flat-bottomed plates and cultured for 24 h before exposure to various concentrations of cisplatin for 72 h. Cell Counting Kit-8 solution

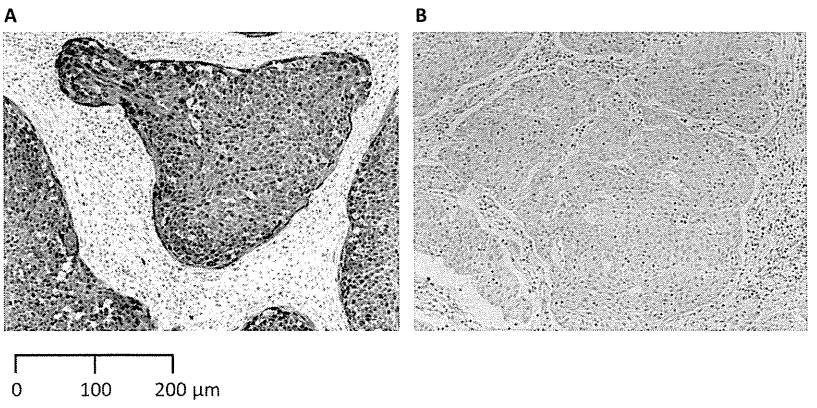

Figure 2. Representative IHC staining of p16 in OPSCC tumor specimens. Tumors were classified as either positive (A) or negative (B) for p16 expression. Scale bar, 200 μm. IHC, immunohistochemistry; OPSCC, oropharyngeal squamous cell carcinoma.

(Dojindo, Kumamoto, Japan) was then added to each well, and the cells were incubated for 3 h at 37°C before measurement of absorbance at 490 nm with a Multiskan Spectrum instrument (Thermo Labsystems, Boston, MA). Absorbance values were expressed as a percentage of that for nontreated cells, and the median inhibitory concentration (IC_{50}) of cisplatin for inhibition of cell growth was determined.

Statistical analysis

Patient characteristics were compared between individuals positive or negative for HPV DNA with Student's two-tailed *t*-test or the chi-square test. Survival curves were constructed by the Kaplan–Meier method and were compared with the log-rank test. The impact of various factors on survival was evaluated by multivariate analysis according to the Cox regression model. Concordance between HPV DNA and p16 assay results was assessed with the kappa statistic (κ) and Spearman correlation. Statistical analysis was performed with the use of IBM SPSS statistics software version 20 (SPSS Inc., IBM, Chicago, IL). A *P*-value of <0.05 was considered statistically significant.

Results

Patient characteristics

The characteristics of the 104 studied patients are listed in Table 1. The median age of the patients was 64 years,

Table 1. Characteristics of the 104 study patients according to HPV DNA and p16 status.

		HPV DNA(+) (n = 40, 38%), n (%)		HPV DNA(−) (n = 64, 62%), n (%)		HPV DNA(+) vs. HPV DNA(−)
	All patients (n = 104), n (%)	p16(+) (n = 32)	p16(−) (n = 8)	p16(+) (n = 7)	p16(−) (n = 57)	(P-value)
Sex						
Male	81 (78)	23 (72)	6 (75)	5 (71)	47 (82)	0.329
Female	23 (22)	9 (28)	2 (25)	2 (29)	10 (18)	
Age (years)						
Median	64	60	66	71	65	0.276
Range	35–80	36–75	35–71	59–77	38–80	
T classification						
1–2	70 (67)	23 (72)	6 (75)	6 (86)	35 (61)	0.372
3–4	34 (33)	9 (28)	2 (25)	1 (14)	22 (39)	
N classification						
0	29 (28)	3 (9)	3 (38)	1 (14)	22 (39)	0.021
1–3	75 (72)	29 (91)	5 (63)	6 (86)	35 (61)	
Stage						
I–III	27 (26)	6 (19)	3 (38)	1 (14)	17 (30)	0.524
IV	77 (74)	26 (81)	5 (63)	6 (86)	40 (70)	
Tobacco usage						
Never smoker	39 (38)	21 (66)	1 (13)	5 (71)	14 (25)	0.010[1]
<40 pack-years	27 (26)	9 (28)	2 (25)	0 (0)	16 (28)	
>40 pack-years	38 (37)	2 (6)	5 (63)	2 (29)	27 (47)	
Tumor location						
Tonsil	60 (58)	26 (81)	5 (63)	5 (71)	24 (42)	0.002[2]
Posterior wall	6 (6)	0 (0)	0 (0)	0 (0)	6 (11)	
Lateral wall	4 (4)	2 (6)	0 (0)	1 (14)	1 (2)	
Base of tongue	13 (13)	4 (13)	0 (0)	1 (14)	8 (14)	
Anterior palatine arch	13 (13)	0 (0)	2 (25)	0 (0)	11 (19)	
Unknown	8 (8)	0 (0)	1 (13)	0 (0)	7 (12)	
Initial therapy[3]						
RT(+)	85 (82)	27 (84)	8 (100)	7 (100)	43 (75)	0.426
RT(−)	19 (18)	5 (16)	0 (0)	0 (0)	14 (25)	

P-values were calculated with Student's two-tailed *t*-test for age and the chi-square test for other variables. HPV, human papillomavirus.

[1]Comparison of patients who never smoked versus patients with a smoking history.

[2]Comparison between tonsil and other sites.

[3]RT(+), treatment with radiation, including radiation therapy alone (n = 3), chemoradiotherapy alone (n = 13), or surgery followed by radiation therapy (n = 46) or by chemoradiotherapy (n = 23); RT(−), treatment without radiation, including surgery alone (n = 11), surgery followed by chemotherapy (n = 1), chemotherapy alone (n = 4), and best supportive care (n = 3).